Local linearity, coherent structures, and scale-to-scale coupling in turbulent flow

Lei Fang,[1] Sanjeeva Balasuriya,[2] and Nicholas T. Ouellette[1,*]
[1]*Department of Civil and Environmental Engineering, Stanford University, Stanford, California 94305, USA*
[2]*School of Mathematical Sciences, University of Adelaide, Adelaide, South Australia 5005, Australia*

(Received 20 July 2018; published 4 January 2019)

Turbulent and other nonlinear flows are highly complex and time dependent, but are not fully random. To capture this spatiotemporal coherence, we introduce the idea of a linear neighborhood, defined as a region in an arbitrary flow field where the velocity gradient varies slowly in space over a finite time. Thus, by definition, the flow in a linear neighborhood can be approximated arbitrarily well by only a subset of the fluid-element trajectories inside it. This slow spatiotemporal variation also allows short-time prediction of the flow. We demonstrate that these linear neighborhoods are computable in real data using experimental measurements from a quasi-two-dimensional turbulent flow and find support for our theoretical arguments. We also show that our kinematically defined linear neighborhoods have an additional dynamical significance, in that the scale-to-scale spectral energy flux that is a hallmark of turbulent flows behaves differently inside the neighborhoods. Our results add additional support to the conjecture that turbulent flows locally tend to transport energy and momentum in space or in scale but not both simultaneously.

DOI: 10.1103/PhysRevFluids.4.014501

I. INTRODUCTION

Turbulent flows mix very efficiently. However, although turbulence tends to enhance mixing globally, at a local level mixing is typically not spatiotemporally uniform even in a turbulent flow. Instead, there are often distinguished spatiotemporally compact regions of fluid elements, commonly known as coherent structures, that evolve without significantly mixing with the surrounding fluid [1]. We will refer to such behavior as kinematic coherence, since the coherence is defined with respect to the (Lagrangian) kinematic evolution of fluid elements according to the Eulerian velocity field. However, the concept of coherence can be extended to other transported dynamical fields such as turbulent kinetic energy, which also displays coherently evolving regions [2]. Of particular relevance in turbulent flows is the flux of energy between scales, which is also spatiotemporally nonuniform and well correlated with the flow [3]. Few links, however, have yet been made between concepts of kinematic and dynamical coherence [2,4].

Coherent structures have been studied from different perspectives for many different reasons, including modeling, flow control, and transport. Here we focus on concepts of coherence as they relate to transport and mixing. In the past few decades, there has been a proliferation of techniques aimed at finding and characterizing regions of coherent transport based on the flow kinematics, typically in the Lagrangian framework [1,2,5]. Many of these diagnostic methods are based on physical intuition for what properties a kinematic coherent structure may be expected to have [5]; these include stable and unstable manifolds [6], finite-time Lyapunov exponents (FTLEs) [7,8],

*nto@stanford.edu

finite-size Lyapunov exponents [9], mesochronic analysis [10], extremally attractive or repulsive surfaces [1], flow barriers under diffusion [11], and shape coherence [12]. More analytical methods that define coherent structures by solving specified mathematical coherence problems [5] have also been developed, such as those based on transfer operators [13,14], fuzzy clustering [15], spectral clustering [16], and graph coloring [17]. Most of these methods are rooted in the underlying assumptions that fluid elements inside coherent structures should not mix significantly and should move in fairly similar ways over the lifetime of the structure, and their efficacy is validated in the same fashion.

Here we approach coherence from a somewhat different starting point, namely that the behavior of the set of fluid elements inside a coherent structure ought to be predictable from knowing the behavior of just a few of them. Thus, we define this version of coherent structures, which we term linear neighborhoods (LNs), as regions in which using an unsteady but spatially linear approximation to the flow field based on *one* central trajectory is highly accurate across the entire structure. This definition specifically requires the variation of the velocity gradient in the LN to be slow over a finite time. In this way, we generalize our previous work on what we termed hyperbolic neighborhoods [18] by relaxing any requirements of hyperbolicity and by incorporating a timescale during which the LN has predictive power.

In addition to showing that this definition of coherence is computable and reasonable, we also demonstrate its connection to the turbulent flow dynamics. We do this rather than compare our LNs to other definitions of coherent structures (such as those described above) in detail because there is no *a priori* reason why LNs should provide the same information as, say, FTLEs; thus, drawing links with the flow dynamics is more informative than such a comparison. In previous work, we argued that the local, instantaneous spectral energy flux between scales, the hallmark of turbulence, is highly sensitive to the advective history of the flow [19], since advection may upset the delicate alignment between the turbulent stress and the scale-dependent rate of strain that is required for efficient spectral transfer [19,20]. However, since the flow inside LNs is by definition much simpler than in the rest of the domain, we find that the spectral energy flux is enhanced inside these regions the longer they exist. Thus, we identify a dynamical role of these LNs [4] and, with the support of experimental data, make the conjecture that the turbulent dynamics has a tendency to move energy between scales or in space at a single scale, but rarely both at the same time.

We begin below by describing our definition of LNs in Sec. II. In Sec. III we describe our experimental setup and the results of applying the definition to these experimental flows. Then, in Sec. IV, we describe the connections between LNs and the local spectral energy transfer. Finally, in Sec. V, we summarize our results and conclude.

II. DEFINING LINEAR NEIGHBORHOODS

In any complex unsteady flow, most coherent structures will only exist over a finite-time interval. For concreteness, we therefore consider times in an interval $t \in [t_0, t_0 + T]$, with the initial time t_0 and the time of flow T being fixed. Let $\boldsymbol{x}$ be the trajectory of a fluid element and let $\boldsymbol{y}$ be the trajectory of another fluid element that is nearby at the initial time t_0 so that

$$\boldsymbol{y}(t_0) = \boldsymbol{x}(t_0) + \delta\boldsymbol{x}(t_0), \tag{1}$$

where $\delta\boldsymbol{x}(t_0)$ is presumed to be small. Now, because both $\boldsymbol{x}$ and $\boldsymbol{y}$ are trajectories associated with the (unsteady and potentially turbulent) velocity field $\boldsymbol{u}$, they must obey the integral equations

$$\boldsymbol{x}(t_0 + T) = \boldsymbol{x}(t_0) + \int_{t_0}^{t_0+T} \boldsymbol{u}(\boldsymbol{x}(t), t)dt \tag{2}$$

and

$$\boldsymbol{y}(t_0 + T) = \boldsymbol{y}(t_0) + \int_{t_0}^{t_0+T} \boldsymbol{u}(\boldsymbol{y}(t), t)dt. \tag{3}$$

Subtracting Eq. (2) from Eq. (3), we obtain

$$\delta \boldsymbol{x}(t_0 + T) = \delta \boldsymbol{x}(t_0) + \int_{t_0}^{t_0+T} [\boldsymbol{u}(\boldsymbol{y}(t), t) - \boldsymbol{u}(\boldsymbol{x}(t), t)]dt, \tag{4}$$

which is an exact representation of $\delta \boldsymbol{x}(t_0 + T)$. Now, if $\delta \boldsymbol{x}(t_0)$ is small, it is reasonable to make a linear approximation for the velocity difference in Eq. (4). Doing so gives

$$\delta \boldsymbol{x}(t_0 + T) = \delta \boldsymbol{x}(t_0) + \int_{t_0}^{t_0+T} \nabla \boldsymbol{u}(\boldsymbol{x}(t), t)[\boldsymbol{y}(t) - \boldsymbol{x}(t)]dt + R, \tag{5}$$

where the remainder term R satisfies

$$R \leqslant C \sup_{t\in[t_0,t_0+T]} |\delta \boldsymbol{x}(t)|^2, \tag{6}$$

where the notation $|\cdot|$ denotes the length of a vector, for some constant C that in general will depend on T and the smoothness and boundedness of $\boldsymbol{u}$.

At the initial time instant t_0, we seek a neighborhood around the point $\boldsymbol{x}(t_0)$ such that after trajectories have evolved to time $t_0 + T$, the spatially linear approximation in Eq. (5) obtained by neglecting the error term R is acceptable. In other words, we require the linear approximation for $\delta \boldsymbol{x}(t_0 + T)$ in Eq. (5) with $R = 0$ to be much larger than R. Since R can be exactly obtained by comparing Eq. (4) with Eq. (5), we arrive at the condition

$$\begin{aligned} &\left| \int_{t_0}^{t_0+T} \nabla \boldsymbol{u}(\boldsymbol{x}(t), t)[\boldsymbol{y}(t) - \boldsymbol{x}(t)]dt \right| \\ &\quad \gg \left| \int_{t_0}^{t_0+T} \{\boldsymbol{u}(\boldsymbol{y}(t), t) - \boldsymbol{u}(\boldsymbol{x}(t), t) - \nabla \boldsymbol{u}(\boldsymbol{x}(t), t)[\boldsymbol{y}(t) - \boldsymbol{x}(t)]\}dt \right|. \end{aligned} \tag{7}$$

This condition requires that the linear estimate of the displacement $\delta \boldsymbol{x}(t_0 + T) = \boldsymbol{y}(t_0 + T) - \boldsymbol{x}(t_0 + T)$ be very good, meaning that we can obtain the final-time deviation $\delta \boldsymbol{x}(t_0 + T)$ with high fidelity knowing only the initial displacement $\delta \boldsymbol{x}(t_0)$ and the trajectory $\boldsymbol{x}$.

We can therefore define the LN $N_{E,T}(t_0)$ of a point $\boldsymbol{x}(t_0)$ at the initial time t_0 as the set

$$\begin{aligned} N_{E,T}(t_0) := \Bigg\{ \boldsymbol{y} : &\left| \int_{t_0}^{t_0+T} \nabla \boldsymbol{u}(\boldsymbol{x}(t), t)\delta \boldsymbol{x}(t)dt \right| \\ &> E \left| \delta \boldsymbol{x}(t_0 + T) - \delta \boldsymbol{x}(t_0) - \int_{t_0}^{t_0+T} [\nabla \boldsymbol{u}(\boldsymbol{x}(t), t)\delta \boldsymbol{x}(t)]dt \right| \Bigg\}. \end{aligned} \tag{8}$$

This set depends on both the integration time T, which allows us to set the time span over which we require the linear approximation slaved to the trajectory beginning at $\boldsymbol{x}(t_0)$ to hold, and the constant $E \geqslant 1$. We introduce E to allow the precise specification of how good the linear approximation has to be; the larger E is, the more accuracy we are requiring and thus presumably the smaller $N_{E,T}(t_0)$ will be. We call $\boldsymbol{x}$ the center trajectory of the LN and note that all trajectories inside the LN associated with $\boldsymbol{x}$ can be well approximated knowing it alone. This definition differs from our previous work on hyperbolic neighborhoods [18] in that we do not require $\boldsymbol{x}$ to have any particular properties (such as hyperbolicity) and that we explicitly build a timescale of evolution T into the definition of LNs via the integrals. Thus, we are generalizing our previous work [18] both by defining LNs associated with any trajectory in the flow and by requiring nearly linear evolution over some finite-time span; the central idea of looking for regions where linear behavior dominates over nonlinear behavior, however, is qualitatively the same.

This definition is schematically shown in Fig. 1(a). In a two-dimensional flow, the LN of a trajectory will be a three-dimensional tube in space-time as shown in Fig. 1(b); however, for ease of visualization, we will plot LNs at the initial time slice only in what follows (as is commonly done for FTLE fields). One should remember, though, that any trajectory starting inside the LN

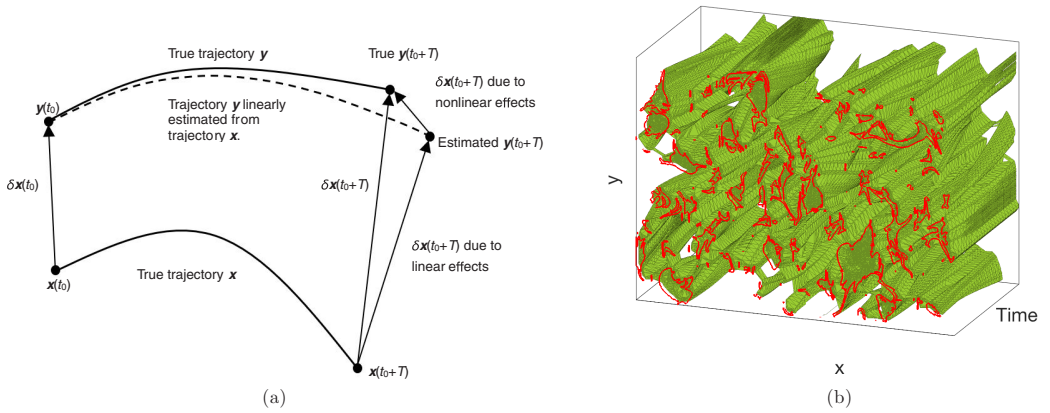

FIG. 1. (a) Schematic of the quantities involved in defining a linear neighborhood. (b) Space-time plot of several LNs found in the experimental data. The red curves show the projection of the LNs at the initial time t_0.

at this initial time slice will still experience the linear flow effect described in Eq. (8) during the entire integration time. Also, we note that the definition of LNs is not restricted to two-dimensional flows. In a three-dimensional flow, the LN will exist in a four-dimensional space-time, but is still completely definable and computable if the velocity field is known.

III. EXPERIMENTS

Both to demonstrate that our definition of LNs is calculable in real flows and to explore what effects LNs may have on the flow dynamics, we have applied the definition to measurements obtained from an experimental quasi-two-dimensional turbulent flow. We briefly describe the experiment below before presenting our results.

A. Experimental methods

As we have presented elsewhere in detail [21–24], our apparatus consists of a thin layer of an electrolytic fluid with lateral dimensions of 86×86 cm^2 driven by electromagnetic forces. Experiments were conducted with a 5-mm layer of a solution of 16% by mass NaCl in water, with a density of $\rho = 1101$ kg/m^3 and a kinematic viscosity of $\nu = 1.25 \times 10^{-6}$ m^2/s. A smooth flat glass floor coated with a hydrophobic wax is used to support the electrolyte and the glass floor is painted black on the underside to improve imaging quality. We float an additional 5-mm fresh-water layer above the electrolyte to create a miscible density interface that defines the horizontal plane of the flow we study.

Under the glass floor, an array of 34×34 permanent magnets with diameters of 12.7 mm, thicknesses of 3.2 mm, and a center-to-center spacing of $L_m = 25.4$ mm (which sets the dominant length scale of the flow) is placed to generate a vertical magnetic field in the apparatus. The strength of each magnet is roughly 600 G on their surfaces and the magnets are arranged in stripes of alternating polarity. A dc electric current of 3.30 A is passed laterally through the electrolyte via a pair of copper electrodes. Because of the orthogonal current and magnetic fields, a Lorentz body force is produced on the fluid. This force is large enough to produce complex spatiotemporal dynamics and weak turbulence, but not so large as to drive significant out-of-plane motions [23]. We define an in-plane Reynolds number $\mathrm{Re} = u' L_m/\nu$, where u' is the in-plane root-mean-square velocity and ν is the kinematic viscosity of the electrolyte, as a nondimensionalization of the strength of the forcing. In the experiments described below, this Reynolds number is 200.

The flow is measured using particle-tracking velocimetry [23,25]. We seed the electrolyte with fluorescent polystyrene tracer particles with diameters of 50 μm [and thus a Stokes number of $O(10^{-4})$] that are small enough to follow the flow accurately [26]. The mass density of the tracer particles lies between that of fresh water and the electrolyte and so the tracer particles stay at the interface. We illuminate the tracer particles with light-emitting diode lamps and image their motion in a subdomain measuring $12L_m \times 9L_m$ in the center of the apparatus at a rate of 60 frames/s with a 4-megapixel camera. We record roughly 30 000 particles per frame, so the velocity fields are highly resolved in space. We work with velocity fields in what follows rather than raw particle trajectories because they give results that are less noisy and with higher spatial resolution [27]. We also postprocess these velocity fields by projecting them onto a basis of streamfunction eigenmodes to remove any slight three-dimensional motion [23].

B. Experimental results

To explore the consequences of our definition of LNs, we generate a set of Lagrangian trajectories for virtual fluid elements started initially on a regular grid by numerically integrating their equations of motion through the measured velocity fields using second-order Runge-Kutta integration. We then apply Eq. (8) to each trajectory to extract its corresponding LN. Note that some LNs are smaller than our experimental resolution and appear to be empty sets.

For convenience, we define t_0 as 0 for all results that we present. Equation (8) has two tuning parameters that can change the LN associated with a given trajectory: E, which specifies the required accuracy of the linear approximation, and T, the length of time for which the LN must persist. In Fig. 2 we fix the integration time T to be one eddy turnover time $T_L = L_m/u'$ and vary E to assess its effect on the LNs. We plot in Fig. 2 a scalar field whose value at a given location is the area of the LN (at the initial time) associated with the trajectory that began at that point. In general, larger LNs are associated with "stronger" linearity, so this field gives a sense of the degree of linearity in the flow. It is clear from Fig. 2 that the degree of linearity in the flow has a nontrivial spatial structure. In general, we also find that the size of the LNs decreases as E increases, as expected; however, some trajectories have a strong enough influence over their neighbors that they continue to dominate a measurably large LN even for relatively large values of E.

In Fig. 3 we again look at the areas of LNs, but now we set $E = 20$ and instead vary the integration time T. Just as one would expect, larger values of T lead to small LNs, since over a longer time span there is a higher likelihood that a given trajectory inside an LN will feel effects from outside that pull it away from the center trajectory. What is intriguing, though, is that qualitatively the spatial structure of the LN area field remains the same even as T is varied. This result suggests that trajectories that evolve in a fairly linear way over short times are likely to continue to experience a linear flow even over longer times. However, this statement only holds in a gross sense; the details of the LN area fields change for different values of T.

Looking only at the scalar field of the areas of the LNs as in Figs. 2 and 3 hides the details of the shapes of the LNs, because these fields reduce the LNs to a single number. We therefore show the full LNs themselves in Fig. 4(a) for $E = 50$ and $T = T_L$. Each curve represents the boundary of one LN and only those LNs with areas larger than our minimum spatial resolution are shown. It is clear that many of these LNs overlap, showing that some regions of the flow are (as one would expect) much less complex than others. This overlapping is also consistent with Figs. 2 and 3, given that those figures show that LNs with large areas tend to cluster together. Building on this observation, in Fig. 4(b) we show the union of these LNs. By construction, any trajectories beginning in regions of the flow covered by this union can be well approximated by only a small subset of trajectories, namely the center trajectories of the LNs that make up this union. (Indeed, to a slightly less well defined level of approximation, one could likely use only one center trajectory for each set of overlapping LNs.) This small subset of center trajectories can then be used to approximate the full flow in the entire domain of the flow covered by the union of LNs.

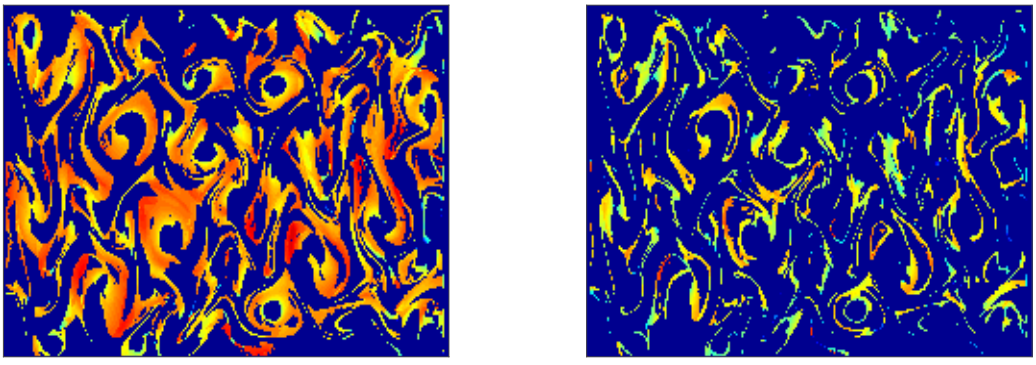

(a) (b)

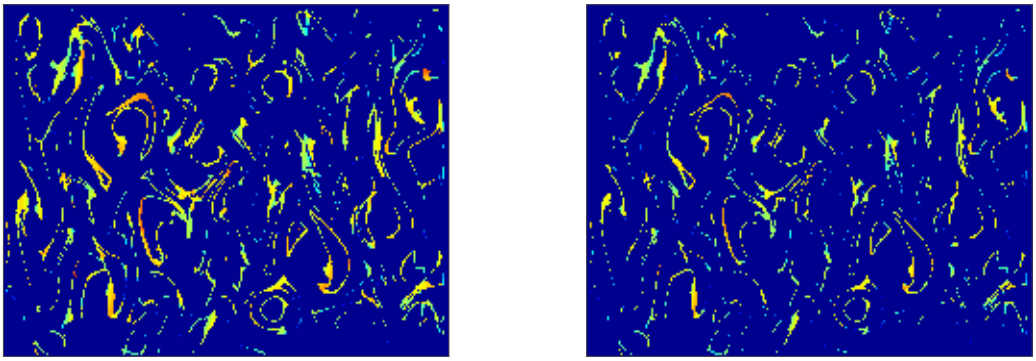

(c) (d)

FIG. 2. Scalar fields of the area of the LN associated with each point at the initial time. The color of each point shows the initial-time area of the LN associated with that point. Colors are on a logarithmic scale and the colormap is uniform for all panels. Data are shown for (a) $E = 5$, (b) $E = 10$, (c) $E = 15$, and (d) $E = 20$. In all cases, $T = T_L$. The full measurement domain is shown, measuring $12L_m \times 9L_m$.

As a final note, we stress here that we have defined LNs based on a somewhat different notion of coherence from what has been used before to detect coherent structures. Thus, there is no reason that our LNs should look the same as what one would find using another method. However, it would also be surprising if the LNs were *completely* different. Thus, to contextualize our results, we show in Fig. 5 two other scalar fields commonly used for detecting coherent structures: the FTLE and the Okubo-Weiss parameter [28,29]. We calculate the FTLE by first computing the flow map $\boldsymbol{\Phi}(\boldsymbol{x}, t_0, T)$, the vector field that gives the position of the fluid element that was at $\boldsymbol{x}$ at time t_0 at the later time $t_0 + T$. The flow map can be used to compute the Cauchy-Green strain tensor

$$C_{ij} = \frac{\partial \Phi_k}{\partial x_i} \frac{\partial \Phi_k}{\partial x_j}, \tag{9}$$

and the FTLE is given by $\ln(\sqrt{\lambda_{\max}})/T$, where $\lambda_{\max}$ is the largest eigenvalue of the Cauchy-Green tensor. The FTLE field is a Lagrangian measure, and ridges of the FTLE field tend to correspond to hyperbolic structures in the flow [1]. The Okubo-Weiss parameter is defined as $\Lambda = -\det \boldsymbol{\nabla u} =$

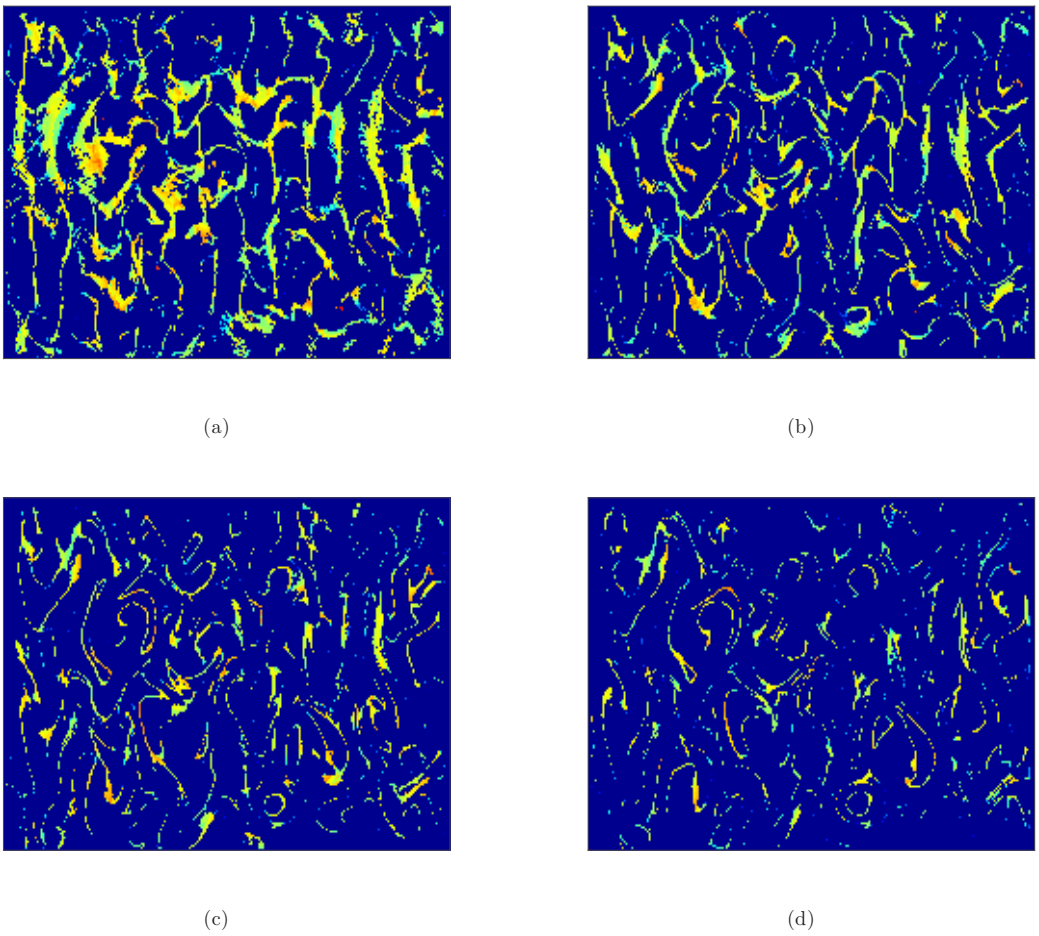

FIG. 3. Scalar fields of the area of the LN associated with each point at the initial time. Colors are on a logarithmic scale and the colormap is uniform for all panels (and the same as in Fig. 2). Data are shown for (a) $T = 0.25T_L$, (b) $T = 0.5T_L$, (c) $T = 0.75T_L$, and (d) $T = T_L$; E is fixed at 20 for all cases. The full measurement domain is shown, measuring $12L_m \times 9L_m$.

$(\omega^2 - s^2)/4$, where s^2 is the square of the strain rate and ω^2 is the square of the vorticity. The Okubo-Weiss parameter is Eulerian and is typically used to partition the flow into regions that are instantaneously dominated by rotation ($\Lambda > 0$) and those dominated by strain ($\Lambda < 0$). There are some qualitative similarities between these two fields and the LNs shown above, but the details are (as one would expect) different. We leave a detailed comparison of the spatial structure of the LNs and these (and other) coherence metrics to future work.

IV. SPECTRAL ENERGY FLUX

Instead, we here explore the connection between LNs and the flow dynamics. As we have defined them, LNs are purely kinematic entities in that they are determined only by *where* fluid elements go with no requirements as to *why* they go there. However, kinematics and dynamics in a real flow are of course linked. Here we show how this linkage is reflected in the dynamical properties of the flow associated with LNs. To do so, we use filter-space techniques (FSTs) to resolve the energetic coupling between scales of motion simultaneously in space and in time [3,19,22,30–36].

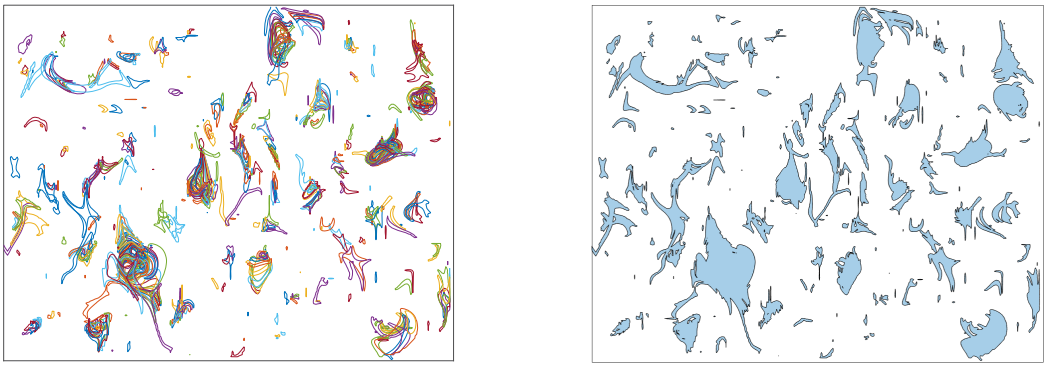

(a) (b)

FIG. 4. (a) Visualization of each LN present in the flow at a single instant of time, for $E = 50$ and $T = T_L$. (b) Union of the LNs shown in (a). The full measurement domain is shown, measuring $12L_m \times 9L_m$.

The idea of an FST is straightforward. We apply a low-pass filter with a cutoff length scale of r to the measured velocity field, which suppresses all the variation on scales smaller than r. Mathematically, we define the filtered velocity field $u_i^{(r)}(x,t)$ as

$$u_i^{(r)}(\boldsymbol{x},t) = \int G^{(r)}(\boldsymbol{x}-\boldsymbol{x}',t)u_i(\boldsymbol{x}',t)d\boldsymbol{x}', \tag{10}$$

where $G^{(r)}$ is a kernel that implements the filter. Filter-space-technique results are fairly insensitive to the precise form of the filter $G^{(r)}$; for concreteness, we here take $G^{(r)}$ to be an isotropic finite impulse response filter constructed from a sharp spectral filter with a cutoff wave number of $2\pi/r$ smoothed with a Gaussian window function to reduce ringing.

After filtering, the equation of motion of the retained kinetic energy $K^{(r)} = (1/2)[u^{(r)}]^2$ can be written as

$$\frac{\partial K^{(r)}}{\partial t} = -\frac{\partial J_i^{(r)}}{\partial x_i} - \nu\frac{\partial u_i^{(r)}}{\partial x_j}\frac{\partial u_i^{(r)}}{\partial x_j} - \Pi^{(r)}, \tag{11}$$

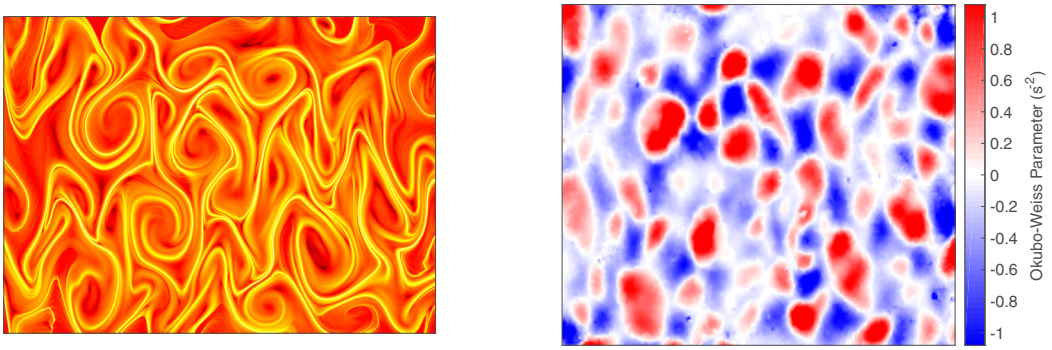

(a) (b)

FIG. 5. (a) The FTLE field computed for an integration time of $T = 3T_L$. (b) Okubo-Weiss parameter. Both fields are shown for the same data as in Figs. 2–4.

where summation is implied over repeated indices and $J_i^{(r)}$ is a spatial current that contains terms similar to those in the equation of motion for the full kinetic energy. The term

$$\Pi^{(r)} = -\left[(u_i u_j)^{(r)} - u_i^{(r)} u_j^{(r)}\right] \frac{\partial u_i^{(r)}}{\partial x_j} = -\tau_{ij}^{(r)} s_{ij}^{(r)} \tag{12}$$

is new and arises from the filtering of the nonlinear term in the kinetic energy equation [22,32,33]. This term acts as a source or sink of kinetic energy in the retained field and so represents the energy transfer between the resolved scales (that is, those larger than r) and the suppressed scales (that is, those smaller than r). Here $\Pi^{(r)}$ can be written as the inner product of $s_{ij}^{(r)}$, the rate of strain of the filtered velocity field, and $\tau_{ij}^{(r)}$, a turbulent stress tensor. Our sign convention is that $\Pi^{(r)} > 0$ indicates energy transfer from large scales to small scales, while $\Pi^{(r)} < 0$ indicates energy transfer from small scales to large scales.

In two-dimensional flow, $\Pi^{(r)}$ can be equivalently expressed in terms of the largest eigenvalue of the (deviatoric) stress tensor $\lambda_\tau^{(r)}$, the largest eigenvalue of the strain rate $\lambda_s^{(r)}$, and the angle $\Theta_{s\tau}^{(r)}$ between the corresponding eigenvectors $\hat{\boldsymbol{e}}_\tau^{(r)}$ and $\hat{\boldsymbol{e}}_s^{(r)}$ as [35–37]

$$\Pi^{(r)} = -2\lambda_s^{(r)} \lambda_\tau^{(r)} \cos 2\Theta_{s\tau}^{(r)}. \tag{13}$$

This expression makes it clear that the alignment between the eigenframes of $\tau_{ij}^{(r)}$ and $s_{ij}^{(r)}$ is essential for determining both the amount of energy transferred between scales and the direction of the transfer, since the eigenvalues $\lambda_\tau^{(r)}$ and $\lambda_s^{(r)}$ are both non-negative. As we have previously suggested, we can therefore think of $|\cos 2\Theta_{s\tau}^{(r)}|$ as an efficiency of the cascade [19,20]. When $\Theta_{s\tau}^{(r)} = \pi/4$, the flux vanishes regardless of the magnitude of the stress or the rate of strain; when $\Theta_{s\tau}^{(r)} < \pi/4$, the energy flux will be directed toward larger scales (inverse cascade), while when $\Theta_{s\tau}^{(r)} > \pi/4$ the energy will flow toward smaller scales (forward cascade).

In our previous work we argued that turbulent advection tends to disturb the delicate angle alignment between the rate of strain and stress that is required for net energy transfer between scales, thus reducing the efficiency of the turbulent cascade [19]. Here we specifically study the evolution of the angle $\Theta_{s\tau}^{(r)}$ for trajectories inside and outside LNs, with the hypothesis that because inside LNs the flow is linear and thus less complex, the advection is not strong enough to disrupt the stress–strain-rate alignment. Hence, we would expect that the longer a trajectory spends inside an LN, the more $\Theta_{s\tau}^{(r)}$ will tend to zero along the trajectory, meaning that the efficiency of spectral transfer will increase. Conversely, we expect that outside the LNs, the more complex advection will keep the stress-strain alignment near its mean value (of about 0.64 radians or 37° [19]).

In Fig. 6 we test this hypothesis by plotting ensemble averages of the time evolution of $\Theta_{s\tau}^{(r)}$ for trajectories that begin inside and outside LNs for several different filter scales r. In this case, we set $T = T_L$ but vary E. As expected, we see that $\Theta_{s\tau}^{(r)}$ decreases for trajectories inside LNs as time evolves for $t < T_L$, the duration within which we define the LN to have predictive capability. This trend is stronger for higher values of E; that is, the more stringent we make the linear approximation, the stronger an effect we see. For times longer than T, the decreasing trend in $\Theta_{s\tau}^{(r)}$ stops, since the trajectories need not remain in LNs past that time. For shorter values of T, this observation also holds, as shown in Fig. 7, where we set $E = 50$ but vary T; note that when T is short, though, the identified LNs may actually persist for a longer time, leading to a somewhat longer time over which the alignment increases.

Thus, we demonstrate a dynamical significance for LNs: Because the flow inside LNs is by construction less complex than that outside the LNs, trajectories inside them display more coherent dynamics that allows the preferential alignment of the stress and the strain rate. Linear neighborhoods are however finite-time structures; thus, as time progresses longer than the lifetime

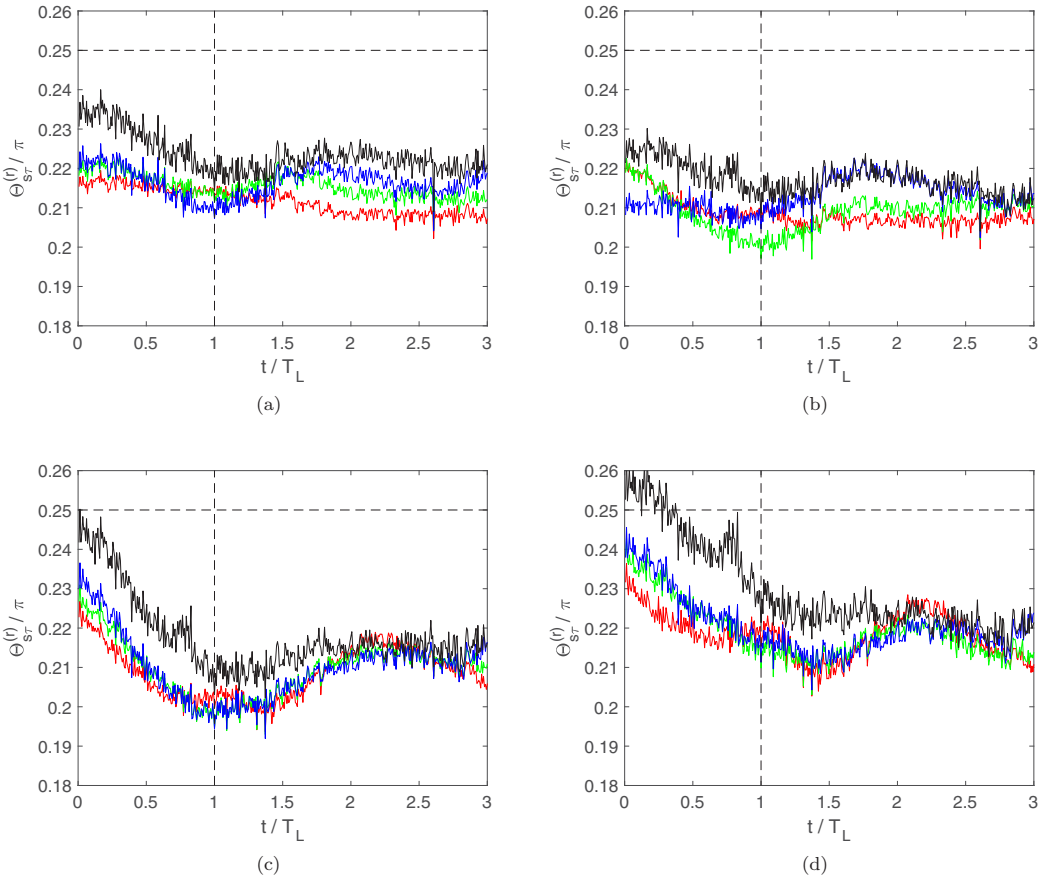

FIG. 6. Evolution of the angle $\Theta_{s\tau}^{(r)}$ between the turbulent stress and strain rate for trajectories that begin inside LNs. The curves have been ensemble averaged over many LNs. Each LN was computed for $T = T_L$, as indicated by the vertical dashed lines. The horizontal dashed lines show $\Theta_{s\tau}^{(r)} = \pi/4$, for which the energy flux vanishes and which separates forward from the inverse energy transfer. In each panel, data are shown for four filter scales in the inverse energy cascade range: $r = 3L$ (red), $r = 3.5L$ (green), $r = 4L$ (blue), and $r = 4.5L$ (black). Each panel shows computations for a different value of E, with (a) $E = 30$, (b) $E = 50$, (c) $E = 70$, and (d) $E = 90$.

of the LN, their influence is lost and trajectories that began inside the LNs return to sharing the spectral properties of a typical trajectory in the flow.

We are thus led to an intriguing conjecture. Inside LNs, the flow is by definition less mixing than it is in the rest of the domain, because the behavior of all of the fluid-element trajectories in the LN can be well predicted by the behavior of just one of them. Since the amount of chaotic or turbulent advection is typically required to mix efficiently, LNs are thus regions where spatial mixing is not particularly strong. Yet, as we have shown, the spectral energy transfer inside LNs is *more* efficient than it is outside them. Since spectral transfer is the redistribution of energy and momentum across scales, this increased efficiency suggests that the flow inside LNs can be thought of as strongly mixing in scale. This finding, that the flow in LNs mixes well in scale but not in space, is in line with our previous results [19] where we showed that large fluctuations in turbulent stress along trajectories leads to a reduction of the cascade efficiency. Thus, we suggest that, in general, turbulent flows mix efficiently in space or in scale, but typically not both at the same time.

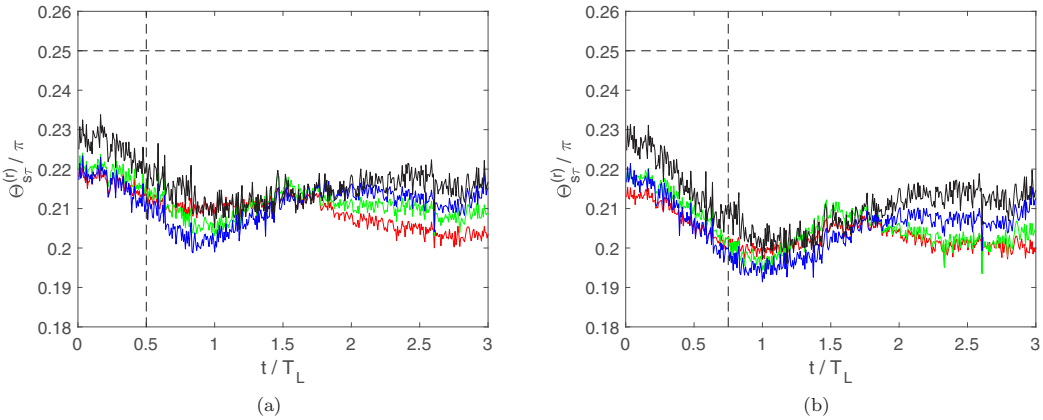

FIG. 7. Evolution of $\Theta_{s\tau}^{(r)}$, as in Fig. 6, for fixed $E = 50$ but for (a) $T = 0.5T_L$ and (b) $T = 0.75T_L$. As in Fig. 6, the horizontal dashed lines show $\Theta_{s\tau}^{(r)} = \pi/4$ and the vertical dashed lines show the time for which the LNs were computed.

V. CONCLUSION

We have described a way of quantifying coherence in turbulent or other unsteady flows by searching for regions in the flow in which a spatially linear approximation for the velocity is adequate over a specified timescale. We have shown that these linear neighborhoods exist in real flows, even when the degree of linearity is constrained to be very high. Unlike some other kinds of coherent structures, however, these LNs also play a dynamical role in the turbulence: Since the flow inside them is less complex, the turbulent stress and strain rate are free to align inside them, leading to efficient spectral energy transfer. We have demonstrated this behavior in an experimental quasi-two-dimensional turbulent flow. Thus, we are led to the conjecture that, on average, turbulent flows tend to efficiently mix in space or between scales, but not both at the same time.

ACKNOWLEDGMENTS

L.F. and N.T.O. acknowledge support from the U.S. National Science Foundation under Grant No. CMMI-1563489. S.B. acknowledges partial support from the Australian Research Council through Grants No. FT130100484 and No. DP170100277.

[1] G. Haller, Lagrangian coherent structures, Annu. Rev. Fluid Mech. **47**, 137 (2015).
[2] S. Balasuriya, N. T. Ouellette, and I. I. Rypina, Generalized Lagrangian coherent structures, Physica D **372**, 31 (2018).
[3] D. H. Kelley and N. T. Ouellette, Spatiotemporal persistence of spectral fluxes in two-dimensional weak turbulence, Phys. Fluids **23**, 115101 (2011).
[4] N. T. Ouellette, On the dynamical role of coherent structures in turbulence, C. R. Phys. **13**, 866 (2012).
[5] A. Hadjighasem, M. Farazmand, D. Blazevski, G. Froyland, and G. Haller, A critical comparison of Lagrangian methods for coherent structure detection, Chaos **27**, 053104 (2017).
[6] S. Balasuriya, *Barriers and Transport in Unsteady Flows: A Melnikov Approach* (SIAM, Philadelphia, 2016).
[7] G. Haller and G. Yuan, Lagrangian coherent structures and mixing in two-dimensional turbulence, Physica D **147**, 352 (2000).

[8] G. Haller, Lagrangian coherent structures from approximate velocity data, Phys. Fluids **14**, 1851 (2002).
[9] E. Aurell, G. Boffetta, A. Crisanti, G. Paladin, and A. Vulpiani, Predictability in the large: An extension of the concept of Lyapunov exponent, J. Phys. A: Math. Gen. **30**, 1 (1997).
[10] I. Mezić, S. Loire, V. A. Fonoberov, and P. Hogan, A new mixing diagnostic and Gulf oil spill movement, Science **330**, 486 (2010).
[11] S. Balasuriya and G. Gottwald, Estimating stable and unstable sets and their role as transport barriers in stochastic flows, Phys. Rev. E **98**, 013106 (2018).
[12] T. Ma and E. Bollt, Differential geometry perspective of shape coherence and curvature evolution by finite-time nonhyperbolic splitting, SIAM J. Appl. Dyn. Syst. **13**, 1106 (2014).
[13] G. Froyland, Statistically optimal almost-invariant sets, Physica D **200**, 205 (2005).
[14] G. Froyland and K. Padberg, Almost-invariant sets and invariant manifolds—Connecting probabilistic and geometric descriptions of coherent structures in flows, Physica D **238**, 1507 (2009).
[15] G. Froyland and K. Padberg-Gehle, A rough-and-ready cluster-based approach for extracting finite-time coherent sets from sparse and incomplete trajectory data, Chaos **25**, 087406 (2015).
[16] A. Hadjighasem, D. Karrasch, H. Teramoto, and G. Haller, Spectral-clustering approach to Lagrangian vortex detection, Phys. Rev. E **93**, 063107 (2016).
[17] K. L. Schlueter-Kuck and J. O. Dabiri, Coherent structure coloring: identification of coherent structures from sparse data using graph theory, J. Fluid Mech. **811**, 468 (2017).
[18] S. Balasuriya, R. Kalampattel, and N. T. Ouellette, Hyperbolic neighbourhoods as organizers of finite-time exponential stretching, J. Fluid Mech. **807**, 509 (2016).
[19] L. Fang and N. T. Ouellette, Advection and the Efficiency of Spectral Energy Transfer in Two-Dimensional Turbulence, Phys. Rev. Lett. **117**, 104501 (2016).
[20] J. G. Ballouz and N. T. Ouellette, Tensor geometry in the turbulent cascade, J. Fluid Mech. **835**, 1048 (2018).
[21] L. Fang and N. T. Ouellette, Multiple stages of decay in two-dimensional turbulence, Phys. Fluids **29**, 111105 (2017).
[22] Y. Liao and N. T. Ouellette, Spatial structure of spectral transport in two-dimensional flow, J. Fluid Mech. **725**, 281 (2013).
[23] D. H. Kelley and N. T. Ouellette, Onset of three-dimensionality in electromagnetically forced thin-layer flows, Phys. Fluids **23**, 045103 (2011).
[24] L. Fang and N. T. Ouellette, Influence of lateral boundaries on transport in quasi-two-dimensional flow, Chaos **28**, 023113 (2018).
[25] N. T. Ouellette, H. Xu, and E. Bodenschatz, A quantitative study of three-dimensional Lagrangian particle tracking algorithms, Exp. Fluids **40**, 301 (2006).
[26] N. T. Ouellette, P. J. J. O'Malley, and J. P. Gollub, Transport of Finite-Sized Particles in Chaotic Flow, Phys. Rev. Lett. **101**, 174504 (2008).
[27] G. A. Voth, G. Haller, and J. P. Gollub, Experimental Measurements of Stretching Fields in Fluid Mixing, Phys. Rev. Lett. **88**, 254501 (2002).
[28] A. Okubo, Horizontal dispersion of floatable particles in the vicinity of velocity singularities such as convergences, Deep-Sea Res. Oceanogr. Abstr. **17**, 445 (1970).
[29] J. Weiss, The dynamics of enstrophy transfer in two-dimensional hydrodynamics, Physica D **48**, 273 (1991).
[30] M. Germano, Turbulence: The filtering approach, J. Fluid Mech. **238**, 325 (1992).
[31] S. Liu, C. Meneveau, and J. Katz, On the properties of similarity subgrid-scale models as deduced from measurements in a turbulent jet, J. Fluid Mech. **275**, 83 (1994).
[32] G. L. Eyink, Local energy flux and the refined similarity hypothesis, J. Stat. Phys. **78**, 335 (1995).
[33] M. K. Rivera, W. B. Daniel, S. Y. Chen, and R. E. Ecke, Energy and Enstrophy Transfer in Decaying Two-Dimensional Turbulence, Phys. Rev. Lett. **90**, 104502 (2003).
[34] S. Chen, R. E. Ecke, G. L. Eyink, M. Rivera, M. Wan, and Z. Xiao, Physical Mechanism of the Two-Dimensional Inverse Energy Cascade, Phys. Rev. Lett. **96**, 084502 (2006).

[35] Z. Xiao, M. Wan, S. Chen, and G. L. Eyink, Physical mechanism the inverse energy cascade of two-dimensional turbulence: A numerical approach, J. Fluid Mech. **619**, 1 (2009).

[36] Y. Liao and N. T. Ouellette, Geometry of scale-to-scale energy and enstrophy transport in two-dimensional flow, Phys. Fluids **26**, 045103 (2014).

[37] Y. Liao and N. T. Ouellette, Long-range ordering of turbulent stresses in two-dimensional flow, Phys. Rev. E **91**, 063004 (2015).